Solar wind magnetohydrodynamic turbulence energy transfer rate ordered by magnetic field topology

B. Hnat , * S. C. Chapman, and C. M. Liptrott CFSA, Physics Department, University of Warwick, Coventry CV4 7AL, United Kingdom

N. W. Watkins 10

CFSA, Physics Department, University of Warwick, Coventry CV4 7AL, United Kingdom and Grantham Research Institute on Climate Change and the Environment, London School of Economics and Political Science, London WC2A 2AE, United Kingdom

(Received 12 May 2025; accepted 4 September 2025; published 16 October 2025)

The magnetic field fluctuations that mediate a magnetohydrodynamic turbulent cascade have distinct magnetic topologies and associated energy transfer rates. Magnetic field topology is classified by the magnetic field gradient tensor constructed from solar wind in situ observations by the four Cluster spacecraft tetrahedron on a scale of \sim 40 proton gyroradii. Energy transfer rates are estimated instantaneously from the third-order term. We find on average 25% and up to 60% larger forward energy transfer rates in hyperbolic topology compared to flux ropes/plasmoids. Hyperbolic topology, consistent with reconnection, preferentially contributes to the forward energy cascade in magnetohydrodynamic turbulence in the solar wind. This forward cascade is a candidate mechanism for heating the solar wind.

DOI: 10.1103/9wb2-r437

I. INTRODUCTION

Magnetohydrodynamic (MHD) turbulence plays a key role in astrophysical and laboratory plasmas and is ubiquitous in the solar wind [1]. Evidence for an MHD range of turbulence in in situ satellite observations includes power-law power spectra [2] and stretched exponential tailed distributions of fluctuations [3,4] with higher-order moments that show nontrivial scaling [5,6], which broadly agree with theoretical predictions [6–8]. As the only in situ observations of astrophysical scale turbulence, solar wind satellite observations are extensively studied both to address the fundamental physics of turbulence and to understand how the solar wind is heated, as the MHD range is known to terminate in a second, kinetic range of scaling below ion Larmor scales [9–11].

Single spacecraft observations provide estimates of the turbulent energy transfer rate, to assess the importance of turbulence for heating the solar wind plasma during its advection through the heliosphere [12–14]. Using the theoretical extension of the Yaglom law [15] to a magnetized plasma [16,17] as well as the von Kármán-Howarth (vKH) energy balance equation [18,19], approximately constant positive energy transfer rates, corresponding to a forward cascade, have been identified on MHD scales [20-23] using Taylor's hypothesis. The values found in these studies

Published by the American Physical Society under the terms of the Creative Commons Attribution 4.0 International license. Further distribution of this work must maintain attribution to the author(s) and the published article's title, journal citation, and DOI.

are $\epsilon = 0.1 - 10 \text{ kJ kg}^{-1} \text{ s}^{-1}$. This method has also been applied to scales below the ion gyroscale by including the Hall current contribution [24]. Multispacecraft magnetosheath observations have provided three-dimensional estimates of ϵ [25].

MHD turbulence is intermittent [26] and both observations [27,28] and simulations [29] suggest that this intermittency corresponds to coherent structures. The evolution of these coherent structures can drive energy transfer across spatial scales and convert magnetic energy into heat, in a manner that fundamentally depends on their topology. There are two distinct topological classes of coherent structure, flux ropes/plasmoids, and X-lines and their three-dimensional counterparts facilitating reconnection. Flux ropes can merge to drive an inverse cascade [30,31]. Current sheets can become unstable, breaking up into smaller eddies to drive a forward cascade [32], and these can form at the interfaces of magnetic flux tubes where the energy can be preferentially dissipated. Straining plasma motions [33,34] can generate current sheets [35] and neutral X-lines [36]. Unstable current sheets can disrupt the MHD energy cascade on scales smaller than the ion inertial length d_i [32], modifying the energy transfer rate. Reconnection accelerates particles, directly heating the plasma ([37] and references therein). Understanding how magnetic topology correlates with energy transfer across the turbulent cascade is then central to understanding how these processes on average facilitate energy transfer from large to small spatial scales in order to heat the solar wind.

In this article, we will use Cluster four-spacecraft solar wind in situ observations to classify the topology of coherent structures using the invariants of the magnetic field gradient tensor [38-41], and estimate their associated instantaneous energy transfer rate (or local energy transfer rate [42]).

^{*}Contact author: B.Hnat@warwick.ac.uk

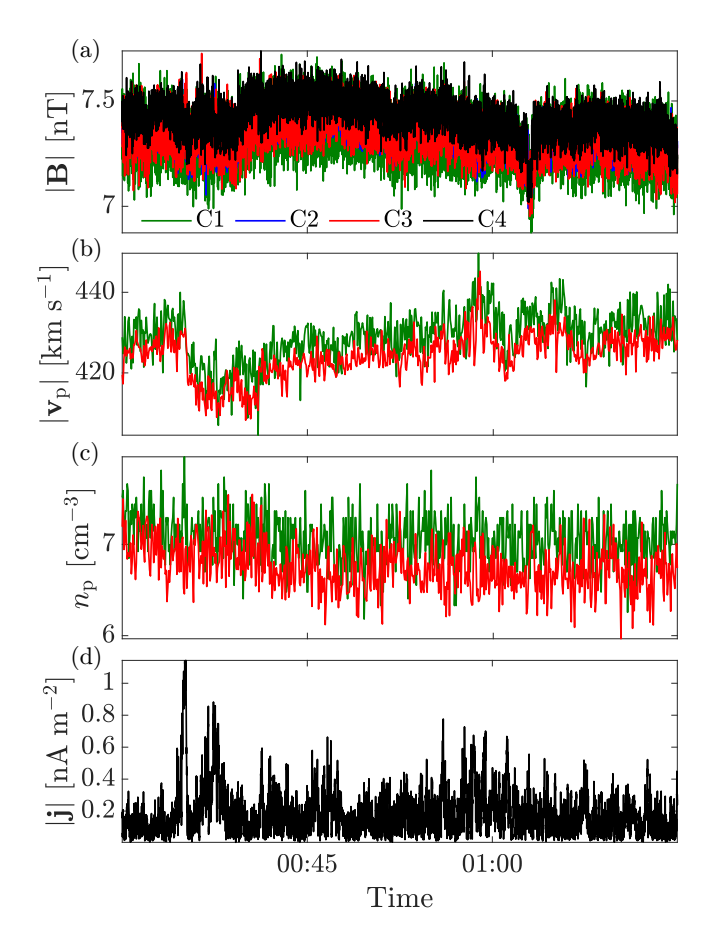


FIG. 1. Time series of *Cluster* observations on 11 February 2003. (a) Magnetic field vector magnitude in the geocentric solar ecliptic (GSE) coordinates at all four *Cluster* spacecraft. (b) Solar wind proton bulk speed \mathbf{v}_p at spacecraft C1 (green) and C3 (red). (c) Ion number density n_p at C1 (green) and C3 (red). (d) Current density magnitude $|\mathbf{j}| = |\nabla \times \mathbf{B}|$.

We find that hyperbolic magnetic topology, that is, three-dimensional (3D) X-line, consistent with reconnection, systematically has instantaneous positive energy transfer rates that are typically 25% and up to 60% greater than those seen in elliptic topology, that is, flux ropes or plasmoids. Negative energy transfer rates are not found to have a single systematic trend with magnetic topology.

II. DATA

The FGM instrument [43] provides vector magnetic field observations at all four spacecraft of the *Cluster* tetrahedron at sampling rate $f_{\rm FGM} \sim 22\,\rm Hz$ and the CIS-HIA instrument [44] provides robust plasma moments on spacecraft pair C1 (Rumba) and C3 (Samba) at sampling rate $f_{\rm HIA} \sim 0.25\,\rm Hz$. Five intervals of solar wind observed by the *Cluster* spacecraft were selected for analysis (Table 1), one of which is summarized in Figs. 1 and 2. The intervals satisfy the following criteria: (1) The *Cluster* tetrahedron is pseudospherical with elongation E < 0.35 and planarity P < 0.35 ([45], Chap. 13) and (2) there is no foreshock contamination, assessed by inspection of the PEACE [46] particle spectra.

FGM observations from the four-spacecraft tetrahedron are low-pass filtered to CIS cadence to directly classify mag-

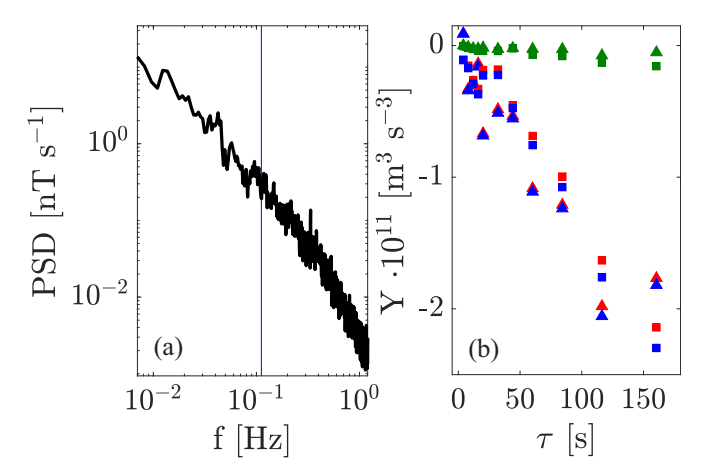


FIG. 2. (a) Trace of the magnetic power spectral density tensor $P = \delta_{ij}B_iB_j$, where i, j = x, y, z from spacecraft C3 for the interval shown in Fig. 1. Blue vertical line indicates the proton gyrofrequency. (b) Variation with scale τ of the Yaglom structure function $Y(\tau)$ (red), Hall-corrected Yaglom structure function $S(\tau)$ (blue), and Hall correction term $H(\tau)$ (green) from spacecraft C1 (triangles) and C3 (squares).

netic field topology contemporaneous with an estimate of the instantaneous energy transfer rate, as the latter requires observations of both magnetic field and plasma moments. We estimate the instantaneous transfer rate independently at spacecraft C1 and C3 using Taylor's hypothesis. To ensure contemporaneous estimates of both magnetic topology and energy transfer rate, we selected intervals for study such that the characteristic size of the tetrahedron L is sufficiently large that the solar wind transit time across the tetrahedron $t_{\rm tr} = \langle L \rangle_t / \langle v_{\rm sw} \rangle_t > 4$ s, the CIS-HIA sampling rate.

III. MAGNETIC FIELD TOPOLOGY

We obtain the coarse-grained magnetic field gradient tensor M_{ij} at the cadence of CIS-HIA and on the $\approx 40d_i$ scale of the Cluster tetrahedron, as detailed in the Appendixes. The tensor invariants [47] of $m = M/\sqrt{M_{mn}M_{mn}}$, given by $3R = -\operatorname{tr}(\mathbf{m}^3)$ and $2Q = \operatorname{tr}(\mathbf{m}^2)$, characterize the full threedimensional magnetic field topology. The signed discriminant of the characteristic equation of m, $D = \frac{27}{4}R^2 + Q^3$, defines two classes of magnetic field topology. Structures with D > 0correspond to elliptic field lines or flux ropes/plasmoids that generalize a two-dimensional O-point to three dimensions. Structures with D < 0 correspond to hyperbolic field lines that generalize a two-dimensional (2D) X-point to three dimensions, that is, the 3D X-line topology of reconnection in three dimensions. These structures become two-dimensional flux ropes (Q > 0) and two-dimensional X lines (Q < 0) as $R \to 0$.

IV. INSTANTANEOUS ENERGY TRANSFER RATE

Our starting point is the Hall-corrected [48] MHD extension of Yaglom's law [16,17]. The Hall MHD assumes magnetized electrons, drifting with the magnetic field line velocity, and nonmagnetized ions. This differential drift leads to an additional current density $j \sim v - v_e$, where v is the

bulk plasma velocity and v_e is the electron velocity. The fluctuations in the current interact with these in the magnetic field contributing extra terms to the energy flux between scales. Yaglom's law relates the mixed third-order structure functions S_r of fluctuations in the velocity δv , the magnetic field δb , and the current δj at length scale r to the scale-independent energy cascade rate ϵ :

$$S_r = Y_r + \frac{1}{2}H_r = -\frac{4}{3}\epsilon r,$$
 (1)

where

$$Y_r = \langle y_r(t) \rangle_t = \langle \delta v_r (|\delta \boldsymbol{v}|^2 + |\delta \boldsymbol{b}|^2) - 2\delta b_r (\delta \boldsymbol{v} \cdot \delta \boldsymbol{b}) \rangle_t,$$

$$H_r = \langle h_r(t) \rangle_t = \langle 2\delta b_r (\delta \boldsymbol{b} \cdot \delta \boldsymbol{j}) - \delta j_r |\delta \boldsymbol{b}|^2 \rangle_t.$$

Here, δv , δb , and δj are the observed time series of fluctuations, or increments, which for a vector quantity a(t) are defined as $\delta a = a(t+\tau) - a(t)$. Quantities δv_r , δb_r , and δj_r are their projections in the direction of the scale separation vector r; magnetic fluctuations are in Alfvén units (i.e., $b = B/\sqrt{\mu_0 n_p m_p}$).

In the solar wind plasma with mean flow velocity $\langle v \rangle$, Taylor's hypothesis assumes that the temporal variations observed in the spacecraft frame of reference are dominated by the Galilean transformation of the longitudinal spatial coordinate. If at the spacecraft location \mathbf{r}_{sc} we observe some quantity $\mathbf{a}(t)$ and at a time τ later $\mathbf{a}(t+\tau)$, then if the time variation in $\mathbf{a}(t)$ is purely due to the convection of quantity \mathbf{a} with the plasma flow, then $\mathbf{a}(t+\tau) = \mathbf{a}(\mathbf{r}_{sc} - \langle v \rangle_t t)$, where $\mathbf{a}(t) = \mathbf{a}(\mathbf{r}_{sc})$. Taylor's hypothesis then translates temporal scale τ between a pair of successive observations in the flow to spatial scale $\mathbf{r} = -\tau \langle v \rangle_t$ so that the fluctuation in some observed quantity \mathbf{a} on scale \mathbf{r} is $\delta \mathbf{a} \equiv \mathbf{a}(t+\tau) - \mathbf{a}(t)$. We estimate $\langle v \rangle_t$ as the average of the solar wind velocity over the data interval.

We then identify an instantaneous energy transfer rate $\varepsilon_L(t)$ such that $\langle \varepsilon_L(t) \rangle_t = \epsilon$ at the scale of the tetrahedron r = L. The observational time series give

$$s_L(t) = y_L(t) + \frac{1}{2}h_L(t) = -\frac{4}{3}\varepsilon_L(t)L.$$
 (2)

Since $S_L = \langle s_L(t) \rangle_t = -(4/3)\epsilon L$, the time series of instantaneous energy transfer rate is given by $\varepsilon_L(t) = (3/4)s_L(t)/(\tau \langle \mathbf{v} \rangle_t)$.

Equation (1) is valid when the inertial range of fluctuations can be clearly identified, that is, when the term that is third order in fluctuations dominates all other terms in the vKH equation. The intermittency of the MHD dissipation [29] implies a slow convergence of the averages of $\varepsilon_L(t)$. MHD turbulence is also anisotropic, with fluctuations in the plane perpendicular to the mean magnetic field dominating the nonlinear energy transfer. It has been found that applying isotropic Yaglom's law to anisotropic MHD simulated turbulence may lead to significant error in the average ϵ , up to 50% [49]. Thus, while the averages of the instantaneous energy transfer rate quoted here are most likely not fully converged, we can still identify clear trends in the distribution in (R, Q) space underlying this average.

We obtain $\varepsilon_L(t)$ from C1 and C3 as detailed in the Appendixes. Obtaining $\varepsilon_L(t)$ that are contemporaneous with the four-spacecraft-based estimates of magnetic topology then requires that $\tau \lesssim t_{\rm tr}$. This is sufficiently close to the ion gy-

rofrequency, which is ~ 10 s for all intervals, that we include the Hall term correction h_r as above.

Figure 2 plots (1) the magnetic field power spectral density and (2) single-point estimates from spacecraft C1 and C3 of the terms in Eq. (1) across multiple temporal scales τ for the data interval shown in Fig. 1. The figure shows a power-law range in the power spectrum and an inverse linear dependence of S_r with temporal scale, seen independently at both spacecraft, as we would expect for an interval of MHD turbulence. The Hall correction only becomes important at small scales, nevertheless we include it throughout.

V. ORDERING OF ENERGY TRANSFER RATE WITH MAGNETIC TOPOLOGY

We now associate the instantaneous energy transfer rate $\varepsilon_L(t)$ with the contemporaneously observed magnetic field gradient tensor invariants R(t) and Q(t), and the signed discriminant D(R,Q) at the timestamps of CIS-HIA and at each spacecraft C1 and C3. To determine the correspondence between magnetic topology and energy transfer rate, we divide this set of observations into two populations, conditioned on the sign of D: elliptic, $\varepsilon_L^{\circ}(t) = \varepsilon_L(t) \mid D > 0$; and hyperbolic, $\varepsilon_L^{\times}(t) = \varepsilon_L(t) \mid D < 0$.

Figure 3 shows quantile-quantile (QQ) plots of these two populations. A point (x_q, y_q) on the QQ plot is one of the quantiles of the second population (y coordinate) plotted against the same quantile of the first population (x coordinate). The quantile index $q = C_x(X < x_q) = C_y(Y < y_q)$ is the parametric coordinate, where C_x and C_y are the cumulative distribution functions (CDFs) for the populations X and Y. The CDFs are inverted to obtain the quantiles using simple linear interpolation [50]. If the two populations are drawn from the same distribution, the QQ plot is a straight y = x line.

Panel (a) of Fig. 3 compares the distributions of $\varepsilon_L(t)$ for all intervals, conditioned on the sign of D: The x axis plots $x = \varepsilon_L^{\circ}(t)$ and the y axis plots $y = \varepsilon_L^{\times}(t)$, which refer to elliptic and hyperbolic topologies, respectively.

There is a clear departure from the y = x line for positive $\varepsilon_L(t)$ indicating larger positive energy transfer rates carried by hyperbolic 3D X-line magnetic field topology, which is consistent with reconnection. Panel (b) shows the same plot for the individual intervals, all of which consistently show this behavior: The positive energy transfer rates are larger in 3D X-line topology, consistent with reconnection, compared to those in the elliptic topology of flux ropes or plasmoids. This trend is approximately linear across all positive values of $\varepsilon_L(t)$, encompassing the (positive) average as well as the large fluctuations. On the other hand, negative energy transfer rates are larger in the 3D X-line topology for some intervals and larger in the flux rope/plasmoid topology for others. As a result, when all intervals are combined [panel (a)], the two topologies have approximately the same distribution of negative $\varepsilon_L(t)$ values.

Panel (c) tests the robustness of this result. Observational uncertainties preclude a precise determination of the sign of D when |D| is sufficiently small, thereby introducing uncertainty in magnetic topology classification. In addition, the division into D>0 and $D\leqslant 0$ is itself approximate under certain field conditions, with the reliability of the classification depending

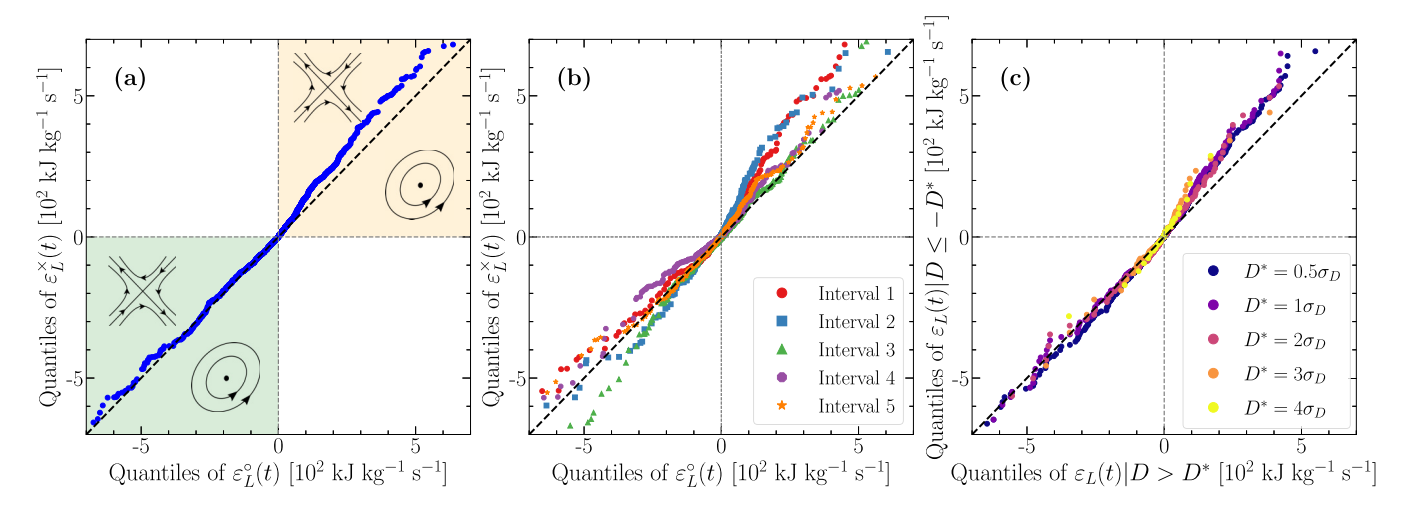


FIG. 3. Quantile-quantile plots compare the distributions of observed $\varepsilon_L(t)$ conditioned on magnetic field topology, elliptical, flux ropes/plasmoids, and 3D X-lines/reconnection as categorized by the sign of the magnetic gradient tensor characteristic D. Panels show QQ plots of (a) all intervals, $\varepsilon_L^{\circ}(t) = \varepsilon_L(t) \mid D > 0$ vs $\varepsilon_L^{\times}(t) = \varepsilon_L(t) \mid D < 0$; (b) as panel (a) for the individual data intervals; (c) all intervals, $\varepsilon_L(t)$ values with $D > D^*$ vs $D < -D^*$. On all panels, the black y = x line indicates that the distributions are the same. The number of points plotted is that of the smallest of the two populations that are compared. Schematics indicate topology in the 2D limit.

on the magnitude of D [51]. To account for both sources of uncertainty, panel (c) replicates panel (a) but excludes $\varepsilon_L(t)$ for which $|D| < D^*$, where D^* is taken as increasing multiples of the sample standard deviation of D. The resulting plots show behavior consistent with panel (a) for all D^* , indicating that our result is robust to both observational error and potential ambiguity in topological classification.

Figure 4 shows the variation of the most extreme energy transfer rate $\varepsilon_L(t)$ across the (R,Q) plane, with the magenta line indicating D=0: Regions above this line correspond to flux rope/plasmoid magnetic topology and those below correspond to 3D X-line topology. Panel (a) displays the top 5% of positive $\varepsilon_L(t)$ and panel (b) displays the top 5% of negative $\varepsilon_L(t)$ by amplitude. There is no apparent preference in $\varepsilon_L(t)$ for 2D $(R\to 0)$ or 3D $(R\neq 0)$ structures. Flux ropes/plasmoids are 64% of the full dataset and are 54% of all structures in panel (a) and 65% in panel (b), so that 3D X-lines are relatively more prevalent at high positive energy transfer rates. These percentages are unbiased as there are roughly the same number of positive and negative $\varepsilon_L(t)$ for both topology types. Panel (c) shows the raw logarithm of counts in the

(R, Q) plane. The topology is more strongly sheared for large |Q| along the D=0 line in the third quadrant; however, the $\varepsilon_L(t)$ do not show significant ordering with this.

Figures 3 and 4 together suggest a systematic preference for larger positive energy transfer rates in 3D X-line structures, with no strong preference in the amplitude of the transfer rate for the "strength" of the magnetic topology, that is, how sheared or three-dimensional the structures are.

The time series of $\varepsilon_L(t)$ are, as we would expect from a turbulent flow, highly intermittent. Thus, while we do obtain an energy transfer rate averaged over all samples here $\langle \varepsilon_L(t) \rangle_t = 3.4 \text{ kJ kg}^{-1} \text{s}^{-1}$, which is consistent with previous estimates [20–23], the width of the distribution is large (see the Appendixes for pdf plots) with correspondingly large spread in the distribution's average, on the order of $\pm 200 \text{ kJ kg}^{-1} \text{s}^{-1}$. Quantitative trends can instead be obtained directly from the QQ plots [Figs. 3(a) and 3(b)]. If the QQ plot trace lies on the y = x line, then the two populations are drawn from the same distribution. However, if part of the QQ trace is displaced from y = x, so that $y \simeq Ax$, then the distribution tail of one population is "stretched" by a factor A relative to the

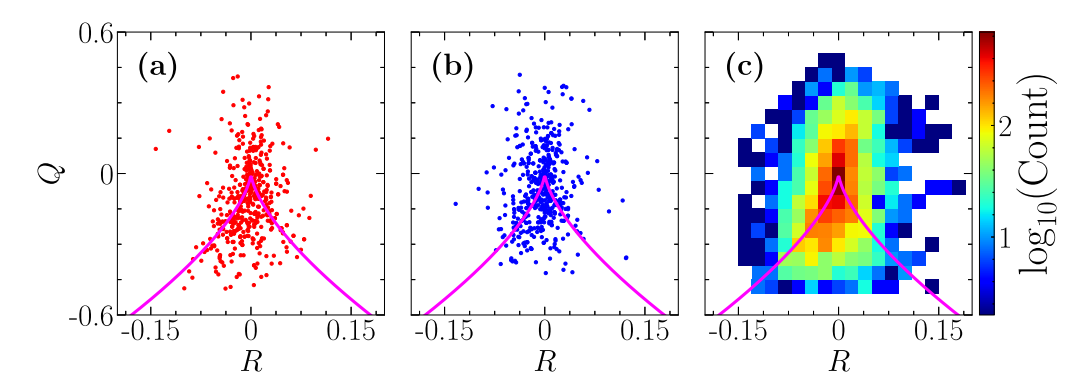


FIG. 4. Energy transfer rate $\varepsilon_L(t)$ plotted in the plane of the (normalized) magnetic field gradient tensor invariants R,Q for (a) the largest 5% of $\varepsilon_L(t) > 0$, (b) the largest 5% by magnitude of $\varepsilon_L(t) < 0$, and (c) logarithm of $\varepsilon_L(t)$ sample counts in each bin. The magenta line indicates the separatrix D=0 in each panel.

distribution of the other population. Assuming this simple linear relationship in the $\varepsilon_L(t) > 0$ region of the QQ plots (see the Appendixes) suggests that 3D X-line topologies have positive instantaneous energy transfer rates of 25% [Fig. 3(a)] and up to 60% [Fig. 3(b)] higher than flux rope/plasmoid topologies.

VI. DISCUSSION AND CONCLUSIONS

We have determined how the instantaneous or local energy transfer rate (see also Ref. [42]) correlates with magnetic field topology. The instantaneous energy transfer rates associated with hyperbolic, 3D X-line (\times) and elliptic, flux rope/plasmoid (\circ) combine under averaging to give the turbulent cascade rate:

$$\epsilon = \langle \varepsilon_L^{\circ}(t) \rangle_t + \langle \varepsilon_L^{\times}(t) \rangle_t. \tag{3}$$

Importantly, while ϵ is a scale-independent cascade rate, the instantaneous energy transfer rates $\varepsilon_L^{\circ,\times}(t)$ and their time averages may depend on scale r and have only been determined at a single scale $r=L\sim 40\,d_i$ here. Our result is that in distribution, $\varepsilon_L^{\times}(t)=A\varepsilon_L^{\circ}(t)$ for $\varepsilon_L^{\circ,\times}(t)>0$, A>1 so that the positive contributions to the overall energy cascade rate ϵ are weighted toward fluctuations with X-line magnetic field topology. In this sense, our result shows that the forward turbulent cascade is carried preferentially by structures with 3D X-line topology. The contribution to the forward cascade rate carried by topology consistent with reconnection is on average 25% and up to 60% higher than that carried by flux ropes/plasmoids.

While the positive correlation between reconnection and enhanced positive energy transfer rates is seen consistently across all the intervals of data that we examined, negative energy transfer rates are in different solar wind intervals associated preferentially with either reconnection or flux rope/plasmoid magnetic topology. This variability in the behavior may be due to the variation in the plasma β of the intervals studied here or it may result from the highly variable nature of coherent structures seen on MHD scales [28]. It may suggest that different turbulence phenomenologies are in operation under different conditions. Further study will elucidate the relationship between energy transfer rates, plasma topology, and the underlying physical mechanisms for turbulence.

The *Cluster* mission characteristic tetrahedron size allows us to probe magnetic topology within the MHD inertial range and construct contemporaneous estimates of $\varepsilon_L(t)$. More recent missions such as the magnetospheric multiscale (MMS) provide a full range of plasma observations at a much higher sampling rates, however, MMS is designed to probe ion kinetic physics and thus has spacecraft configurations smaller than the ion inertial length. Our results underline the importance of proposed and upcoming multispacecraft missions [52] that span both MHD and kinetic scales, which would drive understanding of the physical interpretation of energy transfer and cascade rates across the full MHD and kinetic range of scales in terms of magnetic topology.

ACKNOWLEDGMENTS

This work was partially supported by RCUK grant CG ST/X000915/1. S.C.C., C.M.L. and N.W.W. acknowledge

TABLE I. Data intervals.

| Interval Date and time | eta_p | $ \rho_p\left(d_i\right) $ (km) | $\langle L angle_t d_i^{-1}$ | $	au_{\mathrm{tr}}$ (s) | $\varepsilon_L(t)$ counts |
|---|----------------------|---------------------------------|--------------------------------------|---------------------------------|--------------------------------------|
| 10-Feb-03 18:44-19:01 10-Feb-03 22:30-22:45 11-Feb-03 00:30-01:15 19-Feb-03 23:25-23:40 20-Feb-03 00:34-00:54 | 0.93 0.76 0.28 | , , | 31.3 40.4 44.3 43.3 45.5 | 6.1 7.6 8.9 6.7 6.6 | 1506 1326 4008 1416 1776 |

AFOSR grant FA8655-22-1-7056. We dedicate this paper to the late Tom Chang, constant inspiration, wise mentor and gracious host.

DATA AVAILABILITY

The data supporting this study's findings are available within the article.

APPENDIX A: OBSERVATIONS

Table I gives date and time of each Cluster interval studied in the main text as well as plasma properties during this time. Columns 2–6 list proton plasma β_p , proton gyro-radius ρ_i and proton inertial length d_i , characteristic size of the tetrahedron in the units of the proton inertial length $\langle L \rangle d_i^{-1}$, transit time τ_{tr} of the solar wind across the tetrahedron and the number of samples of the ϵ_L computed for each interval.

APPENDIX B: INSTANTANEOUS ENERGY TRANSFER RATE

For each CIS-HIA 4-s cadence timestamp, at spacecraft C1 and C3, we determine values of the instantaneous energy

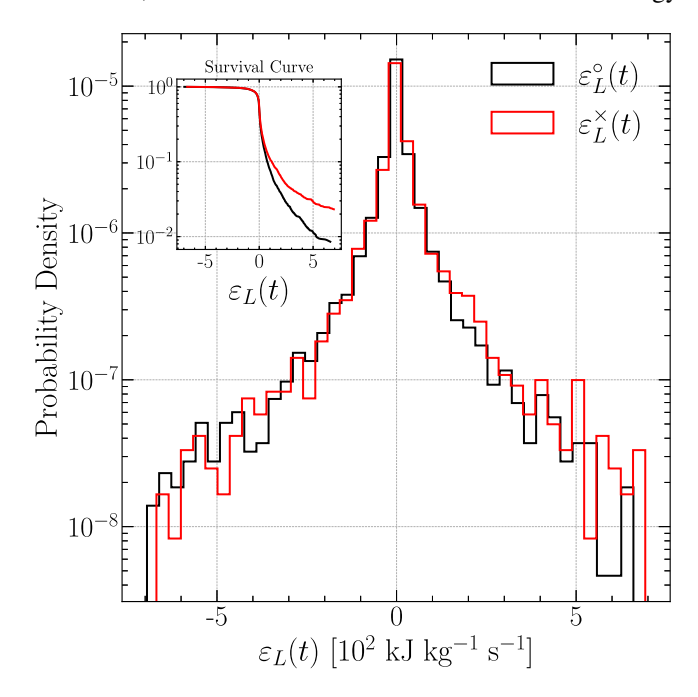


FIG. 5. Probability density of instantaneous energy transfer rates $\varepsilon_L^{\circ}(t)$ and $\varepsilon_L^{\times}(t)$, that is, $\varepsilon_L(t)$ conditioned on the sign of D. Inset: Survival curves (1-CDF) of the same data.

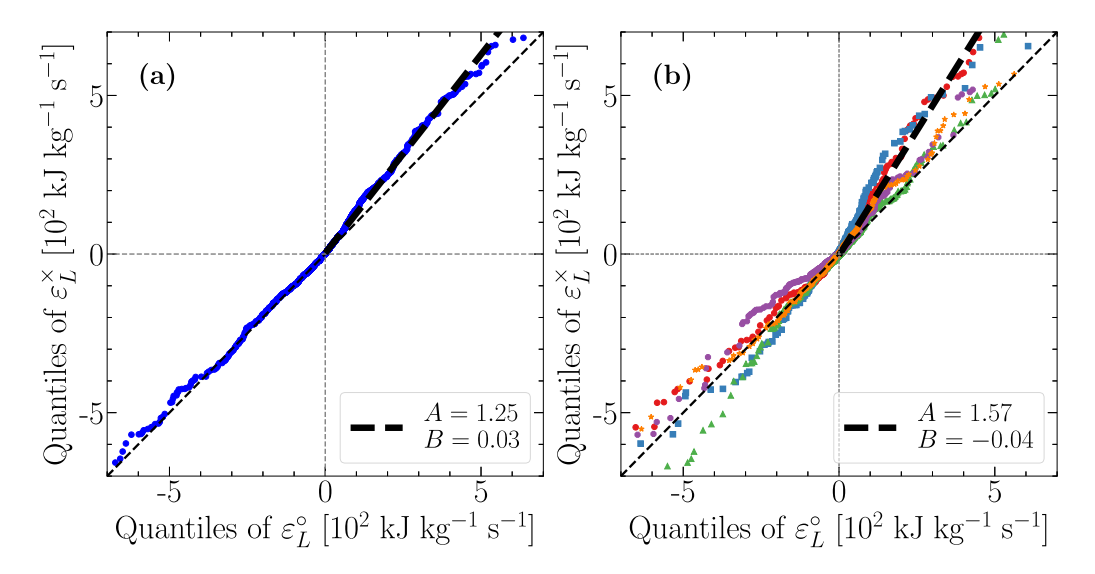


FIG. 6. Regression fitted to the $\varepsilon_L(t) > 0$ region of Figs. 3(a) and 3(b). Fit parameters are provided in the panel legends.

transfer rate $\varepsilon_L(t)$ obtained at all temporal scales that are multiples of the CIS cadence of 4 s. Our analysis requires an estimate that is contemporaneous with the (downsampled to CIS-HIA) magnetic field gradient tensor, that is, on the scale of the four-spacecraft tetrahedron and on timescales $\tau \sim t_{\rm tr}$. We form instantaneous estimates of $\varepsilon_L(t)$ by averaging the two to three values of the energy transfer rate on temporal scales $\tau = 4{\text -}16\,{\rm s}$ closest to each CIS timestamp. We estimate the current density from the magnetic field using the standard curlometer technique [45], that is, $j = \nabla \times b$ in Alfvén units.

APPENDIX C: MAGNETIC FIELD GRADIENT TENSOR

The *Cluster* tetrahedron characteristic length ([45], Chap. 13) spans $\approx 40 \ d_i$ units, which is on MHD scales. A coarse-grained magnetic field gradient tensor on this scale can then be defined as [53]

$$M_{ij} = \frac{1}{V} \int_{V} \frac{\partial B_{i}}{\partial r_{j}} d^{3}r, \tag{C1}$$

where V is the multispacecraft tetrahedron volume. We use least-squares optimization to construct a linear estimate [54] of tensor M subject to the constraint $\nabla \cdot \mathbf{B} = 0$. The tensor invariants [47] of the normalized tensor $\mathbf{m} = \mathbf{M}/\sqrt{M_{mn}M_{mn}}$, given by $3R = -\operatorname{tr}(\mathbf{m}^3)$ and $2Q = \operatorname{tr}(\mathbf{m}^2)$, characterize the magnetic field line topology. The normalization constrains the

invariants to known limits [55]: $R \in [-\sqrt{3}/9, \sqrt{3}/9]$ and $Q \in [-0.5, 0.5]$. An alternative approach is to obtain the invariants from the tensor M and then normalize by the square of the antisymmetric part of M [38,40,41].

Uncertainties in the tensor invariants, based on 0.1 nT uncertainty in magnetic field measurements and 5 km uncertainty in spacecraft position, are between 5% and 9%.

APPENDIX D: DISTRIBUTIONS OF $\varepsilon_L(t)$

For completeness, Fig. 5 shows the probability density histogram of the instantaneous energy transfer rate $\varepsilon_L(t)$, conditioned on the sign of D. The higher probability of large $\varepsilon_L(t) > 0$ for $D \le 0$ is more clearly illustrated in the survival curve inset. The survival functions are 1 - CDF; that is, they show the probability $P(\varepsilon_L(t) > x \mid \text{sgn}(D))$. A strong departure of the distributions is clearly visible for positive $\varepsilon_L(t)$.

To quantify the relative right-side departure from y = x relation associated with positive instantaneous energy transfer rates in the QQ plots of Fig. 3, a simple linear regression was performed on the quantiles for $\varepsilon_L(t) > 0$. Figure 6 shows the resulting fits, y = Ax + B, for (a) all data and (b) interval 2, the latter corresponding to the strongest tail behavior. The slope directly reflects the relative excess of $\varepsilon_L^{\times}(t)$ in hyperbolic regions, indicating approximately 25% and 59% more contribution from hyperbolic structures in each case, respectively.

^[1] R. Bruno and V. Carbone, The solar wind as a turbulence laboratory, Living Rev. Solar Phys. **10**, 2 (2013).

^[2] K. H. Kiyani, K. T. Osman, and S. C. Chapman, Dissipation and heating in solar wind turbulence: From the macro to the micro and back again, Philos. Trans. R. Soc. A 373, 20140155 (2015).

^[3] L. Sorriso-Valvo *et al.*, Intermittency in the solar wind turbulence through probability distribution functions of fluctuations, Geophys. Res. Lett. **26**, 1801 (1999).

^[4] B. Hnat, S. C. Chapman, and G. Rowlands, Intermittency, scaling, and the Fokker-Planck approach to fluctuations of the solar wind bulk plasma parameters as seen by the WIND spacecraft, Phys. Rev. E 67, 056404 (2003).

^[5] S. C. Chapman and B. Hnat, Quantifying scaling in the velocity field of the anisotropic turbulent solar wind, Geophys. Res. Lett. 34, L17103 (2007).

^[6] R. Marino and L. Sorriso-Valvo, Scaling laws for the energy transfer in space plasma turbulence, Phys. Rep. 1006, 1 (2023).

^[7] E. Marsch, Turbulence in the solar wind, in *Reviews in Modern Astronomy*, edited by G. Klare (Springer, Berlin, 1991), Vol. 4, p. 145.

^[8] C. H. K. Chen, Recent progress in astrophysical plasma turbulence from solar wind observations, J. Plasma Phys. 82, 535820602 (2016).

^[9] E. Marsch, Kinetic physics of the solar corona and solar wind, Living Rev. Solar Phys. **3**, 1 (2006).

- [10] G. G. Howes, S. C. Cowley, W. Dorland, G. W. Hammett, E. Quataert, and A. A. Schekochihin, A model of turbulence in magnetized plasmas: Implications for the dissipation range in the solar wind, J. Geophys. Res. 113, A05103 (2008).
- [11] K. H. Kiyani *et al.*, Global scale-invariant dissipation in collisionless plasma turbulence, Phys. Rev. Lett. **103**, 075006 (2009).
- [12] S. R. Cranmer, W. H. Matthaeus, B. A. Breech, and J. C. Kasper, Empirical constraints on proton and electron heating in the fast solar wind, Astrophys. J. 702, 1604 (2009).
- [13] J. E. Stawarz, C. W. Smith, B. J. Vasquez, M. A. Forman, and B. T. MacBride, The turbulent cascade and proton heating in the solar wind at 1 AU, Astrophys. J. 697, 1119 (2009).
- [14] M. K. Verma, D. A. Roberts, and M. L. Goldstein, Turbulent heating and temperature evolution in the solar wind plasma, J. Geophys. Res.: Space Phys. 100, 19839 (1995).
- [15] A. N. Yaglom, On local temperature field structure in a turbulent flow, Dokl. Akad. Nauk SSSR 69, 743 (1949).
- [16] H. Politano and A. Pouquet, Dynamical length scales for turbulent magnetized flows, Geophys. Res. Lett. 25, 273 (1998);.
- [17] G. Gogoberidze, S. Perri, and V. Carbone, The Yaglom law in the expanding solar wind, Astrophys. J. **769**, 111 (2013).
- [18] T. de Kármán and L. Howarth, On the statistical theory of isotropic turbulence, Proc. R. Soc. A 164, 192 (1938); P. Hellinger et al., von Kármán–Howarth equation for Hall magnetohydrodynamics: Hybrid simulations, Astrophys. J. Lett. 857, L19 (2018); Spectral transfer and Kármán–Howarth–Monin equations for compressible Hall magnetohydrodynamics, Astrophys J. 917, 101 (2021).
- [19] H. Politano and A. Pouquet, von Karman-Howarth equation for magnetohydrodynamics and its consequences on third-order longitudinal structure and correlation functions, Phys. Rev. E 57, R21(R) (1998).
- [20] B. T. MacBride, C. W. Smith, and M. A. Forman, The turbulent cascade at 1 AU: Energy transfer and the third-order scaling for MHD, Astrophys. J. 679, 1644 (2008).
- [21] L. Sorriso-Valvo, R. Marino, V. Carbone, A. Noullez, F. Lepreti, P. Veltri, F. R. Bruno, B. Bavassano, and E. Pietropaolo, Observation of inertial energy cascade in interplanetary space plasma, Phys. Rev. Lett. 99, 115001 (2007).
- [22] K. T. Osman, W. H. Matthaeus, K. H. Kiyani, B. Hnat, and S. C. Chapman, Proton kinetic effects and turbulent energy cascade rate in the solar wind, Phys. Rev. Lett. 111, 201101 (2013).
- [23] L. Z. Hadid, F. Sahraoui, and S. Galtier, Energy cascade rate in compressible fast and slow solar wind turbulence, Astrophys. J. **838**, 9 (2017).
- [24] R. Bandyopadhyay, L. Sorriso-Valvo, A. Chasapis, P. Hellinger, W. H. Matthaeus, A. Verdini, S. Landi, L. Franci, L. Matteini, B. L. Giles, and D. J. Gershman, *In situ* observation of Hall magnetohydrodynamic cascade in space plasma, *Phys. Rev.* Lett. 124, 225101 (2020).
- [25] F. Pecora, Y. Yang, W. H. Matthaeus, A. Chasapis, K. G. Klein, M. Stevens, S. Servidio, A. Greco, D. J. Gershman, B. L. Giles, and J. L. Burch, Three-dimensional energy transfer in space plasma turbulence from multipoint measurement, Phys. Rev. Lett. 131, 225201 (2023).
- [26] H. Politano and A. Pouquet, Model of intermittency in magnetohydrodynamic turbulence, Phys. Rev. E 52, 636 (1995);
 W. H. Matthaeus *et al.*, Intermittency, nonlinear dynamics

- and dissipation in the solar wind and astrophysical plasmas, Philos. Trans. R. Soc. A **373**, 20140154 (2015).
- [27] G. Consolini and P. De Michelis, A joint multifractal approach to solar wind turbulence, Fractal Fract. 7, 748 (2023); H. Wu, Honghong *et al.*, Intermittency of magnetic discontinuities in the near-Sun solar wind turbulence, Astrophys. J. Lett. 947, L22 (2023).
- [28] A. Bendt and S. C. Chapman, Ubiquitous threshold for coherent structures in solar wind turbulence, Phys. Rev. R 7, 023176 (2025).
- [29] M. Wan, W. H. Matthaeus, V. Roytershteyn, H. Karimabadi, T. Parashar, P. Wu, and M. Shay, Intermittent dissipation and heating in 3D kinetic plasma turbulence, Phys. Rev. Lett. 114, 175002 (2015); A. Greco, P. Chuychai, W. H. Matthaeus, S. Servidio, and P. Dmitruk, Intermittent MHD structures and classical discontinuities, Geophys. Res. Lett. 35, 19 (2008).
- [30] T. S. Chang, An Introduction to Space Plasma Complexity (Cambridge University Press, Cambridge, UK, 2015).
- [31] A. Pouquet, D. Rosenberg, J. E. Stawarz, and R. Marino, Helicity dynamics, inverse, and bidirectional cascades in fluid and magnetohydrodynamic turbulence: A brief review, Earth Space Sci. 6, 351 (2019); O. Pezzi, D. Trotta, S. Benella, L. Sorriso-Valvo, F. Malara, F. Pucci, C. Meringolo, W. H. Matthaeus, and S. Servidio, Turbulence and particle energization in twisted flux ropes under solar-wind conditions, Astron. Astrophys. 686, A116 (2024).
- [32] S. Boldyrev and N. F. Loureiro, Magnetohydrodynamic turbulence mediated by reconnection, Astrophys. J 844, 125 (2017);
 D. Vech, A. Mallet, K. G. Klein, and J. C. Kasper, Magnetic reconnection may control the ion-scale spectral break of solar wind turbulence, Astrophys. J. Lett. 855, L27 (2018).
- [33] W. H. Matthaeus and D. Montgomery, Selective decay hypothesis at high mechanical and magnetic Reynolds numbers, Ann. N.Y. Acad. Sci. 357, 203 (1980).
- [34] V. Carbone, P. Veltri, and A. Mangeney, Coherent structure formation and magnetic field line reconnection in magnetohydrodynamic turbulence, Phys. Fluids 2, 1487 (1990).
- [35] S. Perri *et al.*, Detection of small-scale structures in the dissipation regime of solar-wind turbulence, Phys. Rev. Lett. **109**, 191101 (2012).
- [36] T. D. Phan *et al.*, Electron magnetic reconnection without ion coupling in Earth's turbulent magnetosheath, Nature (London) 557, 202 (2018); M. S. Davis, T. D. Phan, J. T. Gosling, and R. M. Skoug, Detection of oppositely directed reconnection jets in a solar wind current sheet, Geophys. Res. Lett. 33, 19 (2006).
- [37] B. Hnat, S. C. Chapman, and N. W. Watkins, Topology of turbulence within collisionless plasma reconnection, Sci. Rep. 13, 18665 (2023).
- [38] V. Dallas and A. Alexakis, Structures and dynamics of small scales in decaying magnetohydrodynamic turbulence, Phys. Fluids 25, 105106 (2013).
- [39] M. Materassi and G. Consolini, The stochastic tetrad magnetohydrodynamics via functional formalism, J. Plasma Phys. 81, 495810602 (2015).
- [40] V. Quattrociocchi, G. Consolini, M. F. Marcucci, and M. Materassi, On geometrical invariants of the magnetic field gradient tensor in turbulent space plasmas: Scale variability in the inertial range, Astrophys. J. 878, 124 (2019).

- [41] B. Hnat, S. C. Chapman, and N. W. Watkins, Magnetic topology of actively evolving and passively convecting structures in the turbulent solar wind, Phys. Rev. Lett. **126**, 125101 (2021).
- [42] L. Sorriso-Valvo *et al.*, Local energy transfer rate and kinetic processes: The fate of turbulent energy in two-dimensional hybrid Vlasov–Maxwell numerical simulations, J. Plasma Phys. **84**, 725840201 (2018).
- [43] A. Balogh *et al.*, The *Cluster* magnetic field investigation, Space Sci. Rev. **79**, 65 (1997).
- [44] H. Réme et al., First multispacecraft ion measurements in and near the Earth's magnetosphere with the identical *Cluster* ion spectrometry (CIS) experiment, Ann. Geophys. 19, 1303 (2001).
- [45] G. Paschmann and P. W. Daly, Analysis methods for multi-spacecraft data, ISSI Scientific Reports Series SR-001, ESA/ISSI, Vol. 1 (1998).
- [46] A. D. Johnstone *et al.*, PEACE: A plasma electron and current experiment, Space Sci. Rev. 79, 351 (1997).
- [47] B. J. Cantwell, Exact solution of a restricted Euler equation for the velocity gradient tensor, Phys. Fluids A 4, 782 (1992); C. Meneveau, Lagrangian dynamics and models of the velocity gradient tensor in turbulent flows, Annu. Rev. Fluid Mech. 43, 219 (2011); M. S. Chong, A. E. Perry, and B. J. Cantwell, A general classification of three-dimensional flow fields, Phys. Fluids 2, 765 (1990).
- [48] N. Andrés, S. Galtier, and F. Sahraoui, Exact law for homogeneous compressible Hall magnetohydrodynamics turbulence,

- Phys. Rev. E **97**, 013204 (2018); N. Andrés *et al.*, Energy cascade rate measured in a collisionless space plasma with MMS data and compressible Hall magnetohydrodynamic turbulence theory, Phys. Rev. Lett. **123**, 245101 (2019).
- [49] Y. Wang et al., Strategies for determining the cascade rate in MHD turbulence: Isotropy, anisotropy, and spacecraft sampling, Astrophys. J. 937, 76 (2022); K. T. Osman, M. Wan, W. H. Matthaeus, J. M. Weygand, and S. Dasso, Anisotropic third-moment estimates of the energy cascade in solar wind turbulence using multispacecraft data, Phys. Rev. Lett. 107, 165001 (2011); A. Verdini, R. Grappin, P. Hellinger, S. Landi, and W. C. Müller, Anisotropy of third-order structure functions in MHD turbulence, Astrophys. J. 804, 119 (2015).
- [50] R. J. Hyndman and Y. Fan, Sample quantiles in statistical packages, Am. Stat. 54, 361 (1966).
- [51] P. A. Davidson, Turbulence: An Introduction for Scientists and Engineers, 2nd ed. (Oxford University Press, 2015).
- [52] K. G. Klein *et al.*, HelioSwarm: A multipoint, multiscale mission to characterize turbulence, Space Sci. Rev. **219**, 74 (2023).
- [53] M. Chertkov, A. Pumir, and B. I. Shraiman, Lagrangian tetrad dynamics and the phenomenology of turbulence, Phys. Fluids 11, 2394 (1999).
- [54] R. E. Denton *et al.*, Polynomial reconstruction of the reconnection magnetic field observed by multiple spacecraft, J. Geophys. Res.: Space Phys. 125, e2019JA027481 (2020).
- [55] S. S. Girimaji and C. G. Speziale, A modified restricted Euler equation for turbulent flows with mean velocity gradients, Phys. Fluids 7, 1438 (1995).